THE ROYAL SOCIETY

Received 18 February 2004
Accepted 15 April 2004

Dynamical mechanisms for skeletal pattern formation in the vertebrate limb

H. G. E. Hentschel[1]*, **Tilmann Glimm**[1], **James A. Glazier**[2] **and Stuart A. Newman**[3]

[1]*Department of Physics, Emory University, Maths/Science Center, 400 Dowman Drive, Atlanta, GA 30322, USA*
[2]*Biocomplexity Institute and Department of Physics and Biology, Swain Hall West 159, 727 East Third Street, Indiana University, Bloomington, IN 47405, USA*
[3]*Department of Cell Biology and Anatomy, New York Medical College, Valhalla, NY 10595, USA*

We describe a 'reactor–diffusion' mechanism for precartilage condensation based on recent experiments on chondrogenesis in the early vertebrate limb and additional hypotheses. Cellular differentiation of mesenchymal cells into subtypes with different fibroblast growth factor (FGF) receptors occurs in the presence of spatio-temporal variations of FGFs and transforming growth factor-betas (TGF-βs). One class of differentiated cells produces elevated quantities of the extracellular matrix protein fibronectin, which initiates adhesion-mediated preskeletal mesenchymal condensation. The same class of cells also produces an FGF-dependent laterally acting inhibitor that keeps condensations from expanding beyond a critical size. We show that this 'reactor–diffusion' mechanism leads naturally to patterning consistent with skeletal form, and describe simulations of spatio-temporal distribution of these differentiated cell types and the TGF-β and inhibitor concentrations in the developing limb bud.

Keywords: cell condensation; differentiation; chondrogenesis; vertebrate limb development; reactor–diffusion equations

1. INTRODUCTION

Much recent evidence suggests that the early stages of skeletal pattern formation in the developing vertebrate limb depend on complex dynamics, involving several growth factors and differentiation of cells with receptors that allow response to these factors. These interactions produce tissue domains enriched in the extracellular matrix (ECM) glycoprotein fibronectin, within which the cells accumulate by cell–matrix adhesive interactions (Frenz *et al.* 1989*a*,*b*; Downie & Newman 1994, 1995; see also reviews by Newman & Tomasek (1996) and Hall & Miyake (2000)). Recent *in vitro* work by Miura and coworkers (Miura & Shiota 2000*a*,*b*; Miura *et al.* 2000) suggests that the polypeptide growth and differentiation factor, transforming growth factor-beta (TGF-β) TGF-β2, acts as an 'activator' molecule in a pattern-forming mechanism reminiscent of that proposed by Turing (1952)[1]. Because TGF-β also induces the production of both fibronectin (Leonard *et al.* 1991) and the cell-surface-adhesion protein N-cadherin (Tsonis *et al.* 1994) in limb bud mesenchyme, local elevated concentrations can establish fibronectin-rich domains and cause the cells within these domains to sort out from surrounding mesenchyme. The accumulation of cells at sites of elevated fibronectin deposition followed by direct cell–cell adhesion is called mesenchymal condensation (Hall & Miyake 2000). In the developing limb, cartilage differentiation, or chondrogenesis, follows such condensation. In tetrapod species with bony skeletons, bone later replaces cartilage.

Moftah *et al.* (2002) have recently shown that sites of incipient condensation exert a laterally acting inhibitory effect on chondrogenesis *in vitro* and *in vivo* upon exposure to the ectodermally produced fibroblast growth factors (FGFs), FGF2 and FGF8. Only cells expressing FGF receptor 2 (FGFR2) produce this inhibitor (Moftah *et al.* 2002), and FGFR2 is expressed only at sites of condensation *in vitro* and *in vivo* (Peters *et al.* 1992; Szebenyi *et al.* 1995; Moftah *et al.* 2002). The molecular identity of the inhibitor is unknown[2]. Together, positively autoregulatory (Van Obberghen-Schilling *et al.* 1988; Miura & Shiota 2000*b*), diffusible TGF-β and this laterally acting inhibitor constitute a minimal pattern-forming mechanism which may, in principle, generate the basic vertebrate limb plan (Newman & Frisch 1979; Newman *et al.* 1988; Newman 1996; Kiskowski *et al.* 2004).

This paper develops a set of equations describing the basic features of this biological model of limb development. The equations embody dynamics for establishing the relevant tissue domains for growth and pattern formation, as well as reaction–diffusion-like equations capable of generating roughly stripe-like patterns of cell condensation like those in the developing limb (see figure 1*b*,*c*). In most cases, the dynamics derive from experimentally established interactions between cells and gene products. We will note when our hypotheses go beyond the evidence.

2. MESOBLAST AND ECTODERM

The mesenchymal tissue of the early limb bud, which gives rise to the skeleton and muscles, forms a paddle-shaped mesoblast surrounded by a layer of simple epithelium, the ectoderm. The mitotic index of the differentiating mesoblast during the critical stages of pattern

---

*Author for correspondence (phshgeh@physics.emory.edu).

Proc. R. Soc. Lond. B (2004) **271**, 1713–1722
DOI 10.1098/rspb.2004.2772

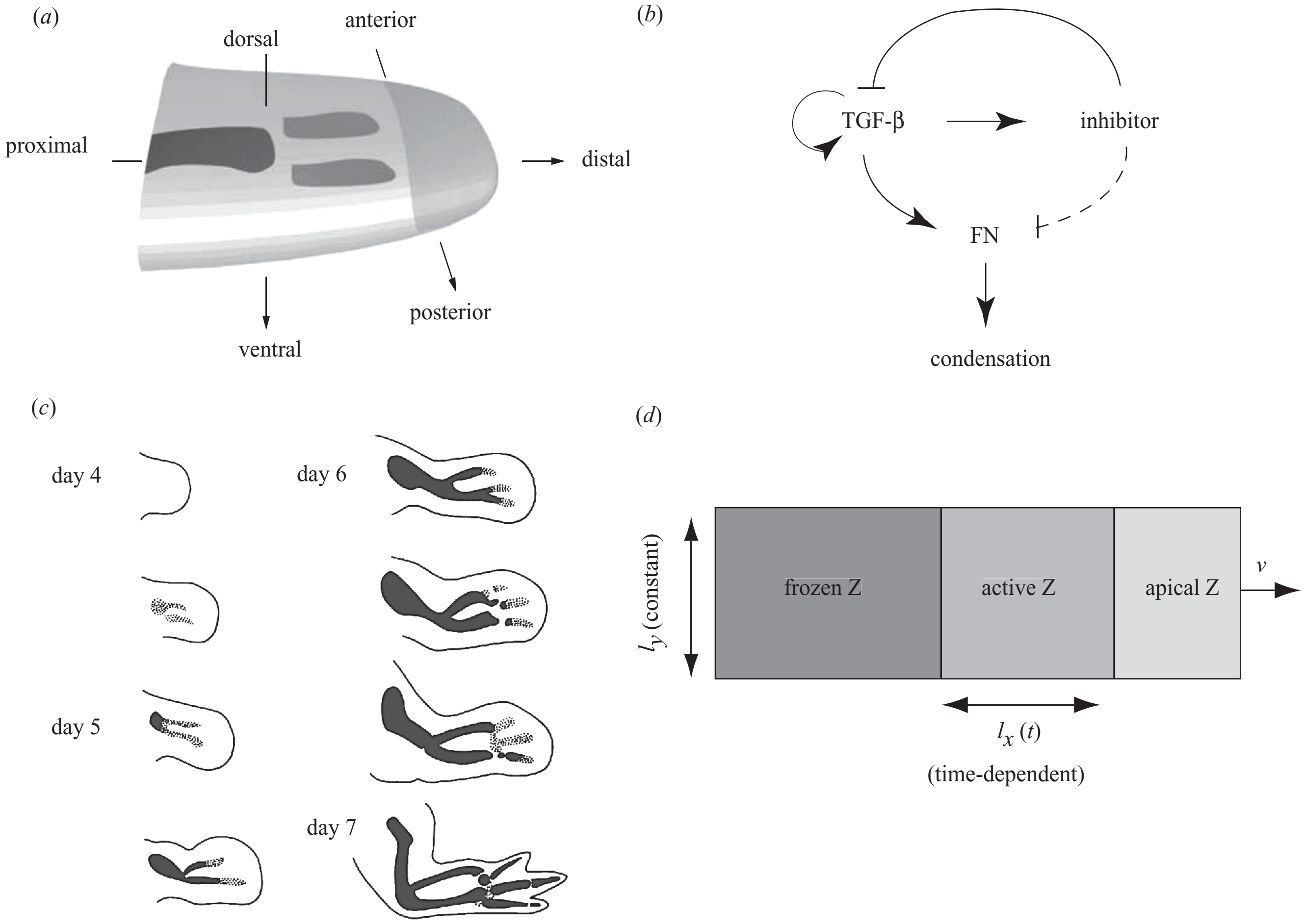

Figure 1. (*a*) A sketch of the embryonic limb bud showing the major developmental axes, the apical zone (light grey), precartilage condensations (medium grey) and cartilage (black). The stage shown is approximately midway through the course of skeletal pattern development. (*b*) A schematic representation of the biochemical circuitry underlying the pattern forming instability described in this paper. Positive autoregulation of TGF-β, induction of fibronectin by TGF-β, promotion of precartilage condensation by fibronectin, and expression of a lateral inhibitor of chondrogenesis from sites of condensation by action of FGFs (not shown) are all supported by experimental evidence. Direct induction of the inhibitor by TGF-β is a hypothesis. The molecular identity of the inhibitor is unknown as is the factor it inhibits. We assume in this paper that it acts directly on TGF-β. (*c*) Progress of chondrogenesis in the chick wing bud between 4 and 7 days of development, shown in cross-section. The stipple represents precartilage; the solid black represents definitive cartilage. Adapted, with changes, from Newman & Frisch (1979). (*d*) Sketch of the model that was used in the simulation scheme to produce figure 2.

formation is essentially uniform along its proximodistal axis before stage 25 (Lewis 1975). The interaction of the distalmost region of the mesoblast (the apical zone) with the apical ectodermal ridge (AER), a narrow band of specialized ectodermal cells located asymmetrically at the tip of the growing limb bud in birds and mammals is, however, essential to proximodistal development of the chick limb bud. The AER keeps the apical-zone mesenchyme in a labile, non-condensed state (Kosher *et al.* 1979) and its removal leads to terminal truncations of the skeleton (Saunders 1948). The entire ectoderm produces FGFs (Martin 1998), but the AER produces a different mix of FGFs from the rest of the limb ectoderm which appears to give it its special role (Niswander *et al.* 1993; Fallon *et al.* 1994).

The apical zone is the only region of the mesoblast with cells that express FGF receptor 1 (FGFR1) (Peters *et al.* 1992; Szebenyi *et al.* 1995). This paper refers to mesenchymal cells that express FGFR1 as R_1 cells. A zone of cell condensation arises proximal to the apical zone, beginning *ca.* 0.3 mm proximal to the AER (see figure 1*a*,*c*). In this zone FGFR1 is downregulated and cells that express FGFR2 appear at the sites of incipient condensation (Peters *et al.* 1992; Szebenyi *et al.* 1995; Moftah *et al.* 2002). We call such FGFR2-expressing cells R_2 cells. To model the establishment of condensations we assume that the AER releases an FGF with concentration c, which diffuses in the growing limb with an effective diffusion constant D, and decays at a rate k, in the ECM:

$$\partial c/\partial t = D\nabla^2 c - kc + \mathcal{J}(\boldsymbol{x}, t), \qquad (2.1)$$

where $\mathcal{J}(\boldsymbol{x}, t)$ represents the flux of FGF. We assume that a boundary flux which equilibrates on a fast time-scale compared with the time-scale for growth, can substitute for the AER. Thus equation (2.1) simplifies to:

$$\nabla^2 c = \kappa^2 c, \qquad (2.2)$$

with $\kappa^2 = k/D$ and $\vec{\nabla} c = (\mathcal{J}/D)\hat{n}$ on the AER boundary. On the anterior and posterior limb-domain boundaries, zero flux boundary conditions are assumed. As release of FGFs can, however, also occur from the dorsal and ventral ectoderm, solving equation (2.2) is numerically challenging if the limb has a complicated shape and the sources of FGFs are distributed asymmetrically on the AER boundary. Equation (2.2) does, however, clearly identify two zones, an apical zone of size $l_{\text{apical}} \approx 1/\kappa$ in which differentiation and consequently condensation is suppressed, and an active zone below the apical zone (see figure 1*d*) in which differentiation and condensation can occur. Newman and coworkers (Newman & Frisch 1979; Newman *et al.* 1988) suggested that the size and shape of this active zone control the number of parallel skeletal primordia. Our simulations based on the present model (see figures 2 and 3, below) suggest that this hypothesis, which is an example of the broader analysis of pattern formation in domains of changing size (Crampin *et al.* 2002*a*,*b*), is biologically plausible, although we have found that other factors, such as the manner in which the active zone grows or shrinks with time, and initial conditions, can strongly influence final pattern selection.

3. PATTERN FORMING INSTABILITIES

The formation of chondrogenic elements *in vitro* and *in vivo* appears to require the interplay between postively autoregulatory and laterally acting inhibitory diffusible factors, resulting in a pattern-forming instability. Here, we present a plausible, but non-unique, set of equations that incorporates this known biology.

We describe the spatio-temporal evolution of the concentration of TGF-β, $c_a(\boldsymbol{x}, t)$, as:

$$\partial c_a/\partial t = \mathcal{J}_a^1 R_1 + \mathcal{J}_a(c_a) R_2 + D_a \nabla^2 c_a - k_a c_i c_a. \qquad (3.1)$$

In equation (3.1) we assume that R_1 cells release TGF-β at a low constant rate $\mathcal{J}_a^1$ and that R_2 cells release TGF-β at a rate $\mathcal{J}_a(c_a)$, corresponding to its upregulation of production in the presence of the local TGF-β concentration, c_a. In the absence of more specific evidence, we assume a Michaelis–Menten form for the TGF-β activator dynamics:

$$\mathcal{J}_a(c_a) = \mathcal{J}_{a,\max}(c_a/c_a^*)^n/[1 + (c_a/c_a^*)^n], \qquad (3.2)$$

where we can select either linear $n = 1$ or quadratic $n = 2$ sigmoidal activation, with a maximum flux $\mathcal{J}_{a,\max}$, saturating at concentrations $c_a \gg c_a^*$. Once produced, TGF-β can then diffuse in the extracellular medium, where D_a is its diffusion constant. The term $k_a c_i c_a$ assumes that the inhibitor binds to the TGF-β forming a non-reactive complex. Such kinetics have been observed for other inhibitors of TGF-β superfamily members (Canalis *et al.* 2003).

The spatio-temporal dynamics of the associated inhibitor concentration $c_i(\boldsymbol{x}, t)$ is then:

$$\partial c_i/\partial t = D_i \nabla^2 c_i - k_a c_i c_a + \mathcal{J}_i(c, c_a)\, R_2, \qquad (3.3)$$

where D_i is the diffusion constant for the inhibitor. We make the simple assumption that inhibitor is removed by the same interaction that sequesters the activator. In a study of the interaction of BMP4 (a member of the TGF-β superfamily) with one its known inhibitors, Noggin, which serves as a prototype for the hypothesized TGF-β-inhibitor interaction here, BMP4 upregulated *noggin* mRNA, but once BMP4 was inactivated by Noggin, *noggin* gene expression was completely suppressed (Sela-Donenfeld & Kalcheim 2002).

We assume that the inhibitor is released by cells expressing FGFR2, and consequently the production of inhibitor is proportional to the local density of R_2 cells (Moftah *et al.* 2002). We have also assumed that the rate at which the inhibitor is released by an R_2 cell is upregulated by both the local FGF concentration and the local concentration of TGF-β. Typically we will assume a hyperbolic dependence for each:

$$\mathcal{J}_i(c, c_a) = \mathcal{J}_{i,\max}(c/c_{\text{sat}})^l/[1 + (c/c_{\text{sat}})^l](c_a/c_{a,\text{sat}})^m/[1 + (c_a/c_{a,\text{sat}})^m]. \qquad (3.4)$$

The dependence on the FGF concentration comes from experiments (Moftah *et al.* 2002), which suggest that FGFR2 cells only express inhibitor in the presence of FGFs. In our *in vivo* simulations we take the FGF concentration to be high close to the AER (defining the apical zone) and to have a lower value in the active zone (see below and figure 1*d*). We assume a hyperbolic form for the dependence of inhibitor production on TGF-β. According to linear stability analysis of the system with the minimal set of assumptions used here, pattern-forming instabilities only occur with such a nonlinear dependence on the activator (see electronic Appendix B). Once an inhibitor molecule is unambiguously identified, therefore, its kinetic dependence on TGF-β can serve as a test of this model.

4. CELL DIFFERENTIATION

Four main types of mesenchymal cell are involved in chick limb skeletal pattern formation: $R_1(\boldsymbol{x}, t)$ denotes the spatially varying density of cells that express FGFR1; $R_2(\boldsymbol{x}, t)$ denotes the spatially varying density of cells that express FGFR2; $R_2'(\boldsymbol{x}, t)$ denotes the spatially varying density of cells deriving from $R_2(\boldsymbol{x}, t)$ which secrete higher levels of fibronectin and display N-cadherin on their surfaces (Oberlender & Tuan 1994); and $R_3(\boldsymbol{x}, t)$ denotes the spatially varying immobile FGF receptor 3-expressing (Szebenyi *et al.* 1995; Ornitz & Marie 2002) cartilage cells. The total density of mobile cells at any spatial point $\boldsymbol{x}$ is thus:

$$R(\boldsymbol{x}, t) = R_1(\boldsymbol{x}, t) + R_2(\boldsymbol{x}, t) + R_2'(\boldsymbol{x}, t). \qquad (4.1)$$

We assume that all mobile cells divide at the same rate. This simplification is in reasonable agreement with the known biology (Lewis 1975). Therefore we shall assume that each mobile differentiated cell type, R_i divides according to the logistic form:

$$r\, R_i(R_{\text{eq}} - R). \qquad (4.2)$$

Note that the form chosen implies that an equilibrium density of all mobile cells R_{eq} is stable in the absence of mesenchymal condensation. Such a stable equilibrium would occur from a suppression of cell division at high cell densities, $R > R_{\text{eq}}$, and apoptosis. Describing the spatio-temporal behaviour of these cell types and the differentiation of one type into another requires four coupled partial differential equations.

(a) *Dynamics of cells expressing fibroblast growth factor receptor 1*

The dynamics for R_1 includes diffusion, haptotaxis, mitosis and differentiation into R_2 cells which we write:

$$\partial R_1/\partial t = D_{\text{cell}}\nabla^2 R_1 - \chi\vec{\nabla}\cdot[R_1\vec{\nabla}\rho] + r\,R_1(R_{\text{eq}} - R) \\ + k_{21}R_2 - k_{12}(c, c_a)R_1. \qquad (4.3)$$

Here, $D_{\text{cell}}\nabla^2 R_1$ represents cellular diffusion. The term $-\chi\vec{\nabla}\cdot[R_1\vec{\nabla}\rho]$ describes condensation as a result of haptotaxis as the cell flux migrates up the fibronectin concentration gradient, where ρ is the fibronectin concentration. The rate of cell division has a logistic form as described above in equation (4.2), where experimentally the rate of doubling is $\sim 1/(rR_{\text{eq}})$ *ca.* 13 h (Lewis 1975). The rate of differentiation $k_{12}(c, c_a)$ of R_1 cells into R_2 cells depends both on the concentrations of FGFs and the activator TGF-β. We assume the rate decreases as the FGF concentration c increases, $\partial k_{12}(c, c_a)/\partial c < 0$ and increases as the activator concentration c_a increases, $\partial k_{12}(c, c_a)/\partial c_a > 0$. A reasonable rate expression consistent with these observations would have a Michaelis–Menten sigmoidal form

$$k_{12}(c, c_a) = k_{12,\max}(c_a/c_a^{**})^q/\{[1 + (c/c^{**})^p][1 + (c_a/c_a^{**})^q]\}, \qquad (4.4)$$

saturating to a maximum value $k_{12,\max}$ at low FGF concentrations $c \ll c^{**}$ and high TFG-β concentrations $c \gg c^{**}$. The rate of differentiation, moreover, decreases in the presence of high concentrations of FGF and becomes very small when $c \gg c^{**}$, as will occur as in the 'apical zone' beneath the AER. The exponents p and q depend on the kinetics of this differentiation. We take the time-scale for R_1 cells to differentiate into R_2 cells in the absence of inhibition to be $1/k_{12,\max}$ or ~5 h, although there is no direct experimental measurement of this rate. We also make the assumption that the reverse process is significantly slower: $1/k_{21}$ ~ 36–48 h.

(b) *Dynamics of cells expressing fibroblast growth factor receptor 2*

The dynamics for R_2 cells which release the inhibitor of TFG-β (see equation (3.3) for the inhibitor kinetics) is taken to be:

$$\partial R_2/\partial t = D_{\text{cell}}\nabla^2 R_2 - \chi\vec{\nabla}\cdot[R_2\vec{\nabla}\rho] + rR_2(R_{\text{eq}} - R) \\ + k_{12}(c, c_a)R_1 - k_{21}R_2 - k_{22}R_2. \qquad (4.5)$$

In addition to diffusing, moving up adhesion gradients by haptotaxis and undergoing cell division, the R_2 cells can differentiate back into R_1 cells and also into R_2' cells. The time-scale for the R_2 cells to differentiate into R_2' cells is $1/k_{22}$ ~ 12 h (Moftah *et al.* 2002). We assume this differentiation is irreversible.

(c) *Dynamics of cells expressing fibronectin*

The dynamics of R_2' cells are crucial to chondrogenesis because these cells produce elevated levels of fibronectin (see equation (5.1)) and have greater cell–cell adhesivity, both of which promote precartilage condensation. We write:

$$\partial R_2'/\partial t = D_{\text{cell}}\nabla^2 R_2' - \chi\vec{\nabla}\cdot[R_2'\,\vec{\nabla}\rho] + r\,R_2'(R_{\text{eq}} - R) \\ + k_{22}R_2 - k_{23}R_2'. \qquad (4.6)$$

Again diffusion, haptotaxis and cell division can occur. In addition, the R_2' cells can differentiate into immobile R_3 cells, where the last term represents this differentiation which we estimate to have a characteristic time-scale of $1/k_{23}$ ~ 18 h.

In the absence of contrary experimental data, we have taken the diffusion constants D_{cell} and the response of the cells to the fibronectin gradients, χ, to be identical in equations (4.3), (4.5) and (4.6). We have also assumed that the haptotactic flux of cells is linear in the fibronectin gradient.

(d) *Dynamics of cells expressing fibroblast growth factor receptor 3*

Finally the R_3 dynamics are assumed to be very simple:

$$\partial R_3/\partial t = k_{23}R_2' + r_3R_3(R_{3,\text{eq}} - R_3). \qquad (4.7)$$

In equation (4.7) we assume that the R_2' cells can differentiate irreversibly into immobile R_3 cartilage cells at a rate k_{23}. We allow these immobile cells to continue to divide, but in general we expect that mitosis will occur at a different rate, r_3, from the rate r, for mobile cells; and we also expect that the equilibrium density of cartilage cells $R_{3,\text{eq}}$ will, in general, differ from that for the mobile cell density R_{eq}.

5. FIBRONECTIN AND MESENCHYMAL CONDENSATION

Haptotaxis, the movement of cells up extracellular adhesion gradients, and direct cell–cell adhesion, drive precartilage mesenchymal condensation (Newman & Tomasek 1996; Hall & Miyake 2000). Haptotaxis requires the deposition of adhesive ECM molecules, in particular fibronectin, in a spatio-temporal pattern (Tomasek *et al.* 1982; Frenz *et al.* 1989*b*; Leonard *et al.* 1991; Downie & Newman 1994, 1995). Fibronectin molecules create adhesive patches which can trap cells diffusing through the ECM (Frenz *et al.* 1989*a*). As the residence time of any randomly translocating cell in a volume of tissue will increase in proportion to the concentration of fibronectin in its immediate microenvironment (Zeng *et al.* 2003), the net result is a flow of cells up adhesive gradients which initiates condensation. Because all cell types can release small amounts of fibronectin, but in the presence of TGF-β R_2' cells release more fibronectin (Leonard *et al.* 1991; Downie & Newman 1995), we take the fibronectin density ρ to obey the kinetic equation:

$$\partial\rho/\partial t = k_b(R_1 + R_2) + k_b'R_2' - k_c\rho, \qquad (5.1)$$

with $k'_b \gg k_b$. In equation (5.1) the fibronectin does not itself diffuse but remains localized in the ECM where it was deposited.

6. A 'BARE BONES' MECHANISM FOR SKELETAL DEVELOPMENT

The known biology, therefore, leads naturally to eight coupled nonlinear partial differential equations: for the FGF concentration c, four cell types R_1, R_2, R_2', R_3, the TGF-β concentration which acts as an activator c_a, an inhibitor c_i and the fibronectin density in the ECM ρ. This 'reactor–diffusion' system[3] is extremely complex. Under certain biologically reasonable assumptions, however, we can employ two powerful mathematical tools: separation of time-scales and gradient expansions (see electronic Appendix A). These biological assumptions are: first, that the overall mobile cell density $R = R_1 + R_2 + R_2'$ changes on a time-scale that is slow compared with cell differentiation; and second, that the pattern gradients are small.

What biological evidence do we possess that the time-scale for differentiation is faster than that for changes in the overall cell density? In lung, it has been shown that fibroblasts' TGF-β exposure substantially increased their production of FGFR2 protein within 30 min of administration, in a dose-dependent fashion (Thannickal *et al.* 1998). By contrast, the period of time between Hamburger–Hamilton stages 24 and 29 (Hamburger & Hamilton 1951), during which the digits of the chicken wing bud first emerge and elongate to an extent of *ca.* 0.5 mm, is *ca.* 50 h. Thus the elements elongate at a rate of ~0.5 mm in 50 h. Because the diameter of a single cell is *ca.* 15 μm, and significant change in the limb pattern is detectable only when 30–40 additional cells condense at the tip of the digit primordium, it is reasonable to assume that FGFR kinetics is faster than overall cell density kinetics. It is also important to understand what cellular time-scales we are comparing here. We are not comparing the time-scale for differentiation to the time-scale for individual cells to move; clearly this later time-scale is faster than the time-scale for differentiation. Rather, what we assume to be slow is the time-scale for the overall macroscopic mobile cellular density to change significantly.

We also assume that the pattern gradients are not too steep. More explicitly, the assumption is made that the gradient terms are small compared with the kinetic terms. This approximation is expected to be valid except in regions of steep spatial gradients such as occur near the edges of skeletal elements. It is, however, precisely in these regions that small-scale phenomena such as cellular adhesion will dominate the biology, and continuum approaches are expected to break down in any event. Thus in the regime in which the continuum description is valid we would expect the gradients to be shallow. The eight equations are thereby reduced to four, which capture the basic features of the spatio-temporal regulation of chondrogenesis:

$$\begin{aligned}
&\nabla^2 c = \kappa^2 c,\\
&\partial c_\mathrm{a}/\partial t = [\mathcal{J}_\mathrm{a}^1 \alpha(c, c_\mathrm{a}) + \mathcal{J}_\mathrm{a}(c_\mathrm{a})\beta(c, c_\mathrm{a})]R + D_\mathrm{a}\nabla^2 c_\mathrm{a} - k_\mathrm{a} c_\mathrm{i} c_\mathrm{a},\\
&\partial c_\mathrm{i}/\partial t = D_\mathrm{i}\nabla^2 c_\mathrm{i} - k_\mathrm{a} c_\mathrm{i} c_\mathrm{a} + \mathcal{J}_\mathrm{i}(c, c_\mathrm{a})\beta(c, c_\mathrm{a})R,\\
&\partial R/\partial t = [D_\mathrm{cell} - (\lambda + \lambda_2\gamma(c, c_\mathrm{a}))R]\nabla^2 R - \lambda_2 \partial\gamma/\partial c_\mathrm{a} R^2 \nabla^2 c_\mathrm{a}\\
&\qquad - \lambda_2 \partial\gamma/\partial c R^2 \nabla^2 c + r\,R(R_\mathrm{eq} - R) - k_{23}\gamma(c, c_\mathrm{a})R.
\end{aligned} \tag{6.1}$$

All symbols previously defined retain their original meanings, whereas the new terms $\alpha(c, c_\mathrm{a})$, $\beta(c, c_\mathrm{a})$, $\gamma(c, c_\mathrm{a})$ represent the fraction of each differentiated cell type in the overall mobile cell density: thus $R_1 = \alpha(c, c_\mathrm{a})R$, $R_2 = \beta(c, c_\mathrm{a})R$ and $R_2' = \gamma(c, c_\mathrm{a})R$. These expressions are known functions of the FGF and TGF-β concentrations (see electronic Appendix A). The variables c_a, c_i and R are all subject to no-flux conditions at the limb boundary.

Certain key features of the dynamics can now be identified. First, the FGF concentration is equilibrated but its distribution strongly depends on the source flux distribution. Second, the idea of a template pattern set up independently by the activator and inhibitor that then controls the mobile cell dynamics also appears as one limiting dynamic of equation (6.1). Such patterning will happen provided the mobile-cell density variations are not too large, in which case we can replace $R \approx R_\mathrm{eq}$ in the activator–inhibitor dynamics. The cells respond to gradients in FGF, gradients in TGF-β and gradients in the cell density R, leading to fluxes in each case $\boldsymbol{j}_\mathrm{total} = \boldsymbol{j}_R + \boldsymbol{j}_\mathrm{ca} + \boldsymbol{j}_\mathrm{c}$. Let us consider each of these gradients in greater detail (in this discussion we shall neglect quadratic terms in the gradient compared with linear terms, assuming the gradients to be small). The gradients in the cell density lead to a flux $\boldsymbol{j}_R = -[D_\mathrm{cell} - (\lambda + \lambda_2\gamma(c, c_\mathrm{a}))R]\,\nabla R$. Its direction is determined by the relative size of cell diffusion compared with haptotaxis. Assuming for the moment that haptotaxis is weak, the flux will be directed down the cell density gradient. Then there is a flux of mobile cells $\boldsymbol{j}_\mathrm{ca} = \lambda_2 \partial\gamma/\partial c_\mathrm{a} R^2 \nabla c_\mathrm{a}$ dependent on gradients of TGF-β in equation (6.1). As $\partial\gamma/\partial c_\mathrm{a} > 0$, this flux is up gradients of TGF-β and mediated by fibronectin through λ_2. Finally there is a flux $\boldsymbol{j}_\mathrm{c} = \lambda_2 \partial\gamma/\partial c R^2 \nabla c$ also mediated by fibronectin down the gradients of FGF, since $\partial\gamma/\partial c < 0$.

We now show below and in electronic Appendix B, that not only is equation (6.1) sufficient to represent a 'bare bones' mechanism for limb skeletal development, in that it incorporates a core set of cellular-biochemical processes known to occur in limb bud mesenchyme, but that simulations in an evolving active zone can, under the appropriate geometical constraints, give rise to a realistically patterned limb skeleton. One interesting result from the linear stability analysis in electronic Appendix B is that while the activator–inhibitor dynamics alone are capable of producing patterns, the inclusion of the cell density facilitates this pattern-formation in the following sense: a pattern always develops at a faster rate in the three-variable system (activator–inhibitor–cells) than it does in the activator–inhibitor system alone; the effect is ultimately a result of the flux $\boldsymbol{j}_\mathrm{ca}$. Moreover, in certain cases, patterns that cannot form in the activator–inhibitor system alone (i.e. for which the homogenous state remains stable), *can*, however, emerge in the full system. The inverse, i.e. that a pattern grows in the activator–inhibitor dynamics system alone, but not in the full system, cannot occur.

7. VARIATIONS OF THE ACTIVE ZONE DURING CELL CONDENSATION

The real shape and growth of a developing limb bud is extremely complex. Not only are the overall external dimensions changing with time, but the interior active zone in which any reactor-diffusion occurs will also be changing as a result of the formation of cartilage and bone proximally, and changes in the dimensions of the apical zone distally. To understand the major consequences of such limb bud growth and form on skeletal development, we will make the following geometric approximations: we treat the limb bud as a parallelpiped of proximodistal dimension $L(t)$ (the time dependence is a result of growth), fixed anteroposterior dimensions ℓ_y and dorsoventral dimension ℓ_z. The proximodistal length $L(t)$ will be taken to consist of three regions. An 'apical zone' of undifferentiated R_1 cells at the distal tip of the limb bud, of size $\ell_\mathrm{apical}(t)$; followed by an interior 'active zone' of length $\ell_x(t)$, which consists of differentiated and condensing cell types; and proximally a 'frozen zone' of cartilage cells, of length $\ell_{\text{frozen}}(t)$, obeying $L(t) = \ell_{\text{apical}}(t) + \ell_x(t) + \ell_{\text{frozen}}(t)$ (see figure 1*d*).

The segmentation of the distal interior domain into an apical zone and an active zone is an approximation which will be valid, provided the distribution of FGFs described by the first equation in (6.1) separates a high FGF concentration under the AER from a low concentration proximally. We use this 'active zone model' as the geometric basis for a linear stability analysis (see electronic Appendix B) and our simulations described below.

The reactor–diffusion dynamics take place in the active zone. The dorsoventral dimension ℓ_z, is typically much smaller than the other length scales, and variations in this dimension will be neglected here, though naturally they will need to be considered if fine structure in the dorsoventral direction is to be studied. If we accept the geometry described above, then the length $\ell_x(t)$ of the active zone in which the differentiated cells, activator and inhibitor interact by the mechanism proposed in equation (6.1) can be expected to have a significant impact on the resulting prepattern created in the limb (Newman & Frisch 1979; Newman *et al.* 1988). The reason why such variations in length result in changes of skeletal patterning, is that the number of standing waves of a heterogeneous distribution of a chemical species formed by a reaction–diffusion mechanism depends both on the scale of the basic pattern set by the magnitude of the biological parameters, and on the space available for this pattern to develop, which is set by the domain size (Newman and Frisch 1979; Crampin *et al.* 2002*a*,*b*).

One way in which the size $\ell_x(t)$ of the active zone can be controlled is through the changes in the apical zone, since $\ell_x(t) = L(t) - \ell_{\text{apical}}(t) - \ell_{\text{frozen}}(t)$. As cells are recruited proximally into the frozen zone $\ell_{\text{frozen}}(t)$ and the proximodistal length of the apical zone $\ell_{\text{apical}}(t)$ decreases as a result of reduced FGF secretion by the AER, the proximodistal length of the active zone $\ell_x(t)$, will vary. As in an earlier model (Newman & Frisch 1979), we shall assume that this length generally decreases with time and acts as a control parameter for the selection of spatial modes. It should be borne in mind, however, that the details of active zone dynamics needs further biological study, and that the coarse-grained description we present here cannot account for the fine details of skeletal structure. It is clear that other gene products (Hox family, Wnts, Sonic hedgehog) and localized sources such as the zone of polarizing activity (ZPA) are essential in sculpting the limb bud shape and determining the finer features of skeletal structure (reviewed in Tickle 2003). A model for the shaping of the limb during its outgrowth that incorporates the effects of some of these factors has been presented by Dillon & Othmer (1999).

8. SIMULATIONS OF CHONDROGENESIS

How does this changing active zone length control the prepattern underlying chondrogenesis? A preliminary answer can be found using linear stability analysis (see electronic Appendix B) which shows that in the active zone, prepatterning can develop provided biological parameters are suitably chosen. Then the basic structure of the skeletal elements turns out to result from bifurcations in this prepattern, which result from dynamic variations in the proximodistal length of the active zone.

Using this active-zone model, we computed solutions to equation (6.1) in a moving rectangular domain (the reduction from a parallelepiped to rectangle is achieved by assuming that all variables are constant in the dorsoventral direction). Inside the active domain, the FGF concentration c is assumed to be a non-zero constant. When a site (x, y) leaves the active zone, the concentrations $c_a(x, y)$, $c_i(x, y)$ and $R(x, y)$ are 'frozen' in the prevailing pattern. This freezing produces the results shown in figure 2.

After the frozen pattern has been selected, further growth in the proximodistal direction is still allowed to occur in the frozen zone. In figure 3 we show typical examples of our simulations including such growth at a constant rate. The skeletal-like patterning is very striking, though naturally a great degree of variability can appear depending on both the choice of biological parameters and the choice of the active zone size. These factors can, of course, be found only from biology, as their values have been shaped by evolution.

To perform these simulations, we first rewrite equation (6.1) (apart from the equation for the FGF distribution which we have argued gives rise to the apical zone and active zone) in dimensionless form. We will use the constant anteroposterior scale ℓ_y, as our unit of length and the TGF-β diffusion time-scale ℓ_y^2/D_a, as our unit of time. Then we introduce new dimensionless variables:

$$\begin{aligned} \tilde{\boldsymbol{x}} &= \boldsymbol{x}/\ell_y, \quad \tilde{t} = t \cdot D_a/\ell_y^2, \quad u(\tilde{t}, \tilde{\boldsymbol{x}}) = c_a(t, \boldsymbol{x})/c_*, \\ & v(\tilde{t}, \tilde{\boldsymbol{x}}) = c_i(t, \boldsymbol{x})/c_*, \quad R(\tilde{t}, \tilde{\boldsymbol{x}}) = R(t, \boldsymbol{x})/R_{\text{eq}}, \end{aligned} \tag{8.1}$$

where c_* is any suitable concentration scale, and we choose the equilibrium cell density, R_{eq}, to scale the cell density variations. For the numerical simulations, we considered the following system of scaled nonlinear partial differential equations (see electronic Appendix B):

$$\frac{\partial u}{\partial t} = g[(\tilde{\mathcal{J}}_a(u)\beta(u) + \tilde{\mathcal{J}}_a^1\alpha(u_{\text{eq}}))R - uv] + \nabla^2 u, \tag{8.2}$$

$$\frac{\partial v}{\partial t} = g[\tilde{\mathcal{J}}_i(u)\beta(u)R - uv] + d\nabla^2 v, \tag{8.3}$$

$$\begin{aligned} \frac{\partial R}{\partial t} &= [d_{\text{cell}} - \tilde{\lambda}_2\gamma(u)R]\nabla^2 R + \tilde{r}R(1 - R) \\ &\quad - \tilde{\lambda}_2 \frac{\partial \gamma}{\partial u}(u_{\text{eq}})R^2\nabla^2 u, \end{aligned} \tag{8.4}$$

where all the parameters appearing in equation (8.2) are now dimensionless ratios of biological length- and time-scales:

$$\begin{aligned} & g = \ell_y^2 k_a c_*/D_a, \; \tilde{\mathcal{J}}_a^1 = \mathcal{J}_a^1 R_{\text{eq}}/k_a c_*^2, \; \tilde{\mathcal{J}}_a(u) = \mathcal{J}_a(c_a, c)R_{\text{eq}}/(k_a c_*^2), \\ & d = D_i/D_a, \; \tilde{\mathcal{J}}_i(u) = \mathcal{J}_i(c_a, c)R_{\text{eq}}/(k_a c_*^2), \\ & d_{\text{cell}} = D_{\text{cell}}/D_a, \; \tilde{\lambda} = \lambda R_{\text{eq}}/D_a, \; \tilde{\lambda}_2 = \lambda_2 R_{\text{eq}}/D_a, \; \tilde{r} = r\ell_y^2 R_{\text{eq}}/D_a. \end{aligned} \tag{8.5}$$

It would be useful to obtain these dimensionless ratios directly from the biological rate constants that we have estimated in this paper. Unfortunately we do not possess a complete list of such parameters (for example the molecular identity of the inhibitor is not known). We have therefore worked backwards and chosen the ratios to exhibit the patterns we desired. Most of the ratios are of order

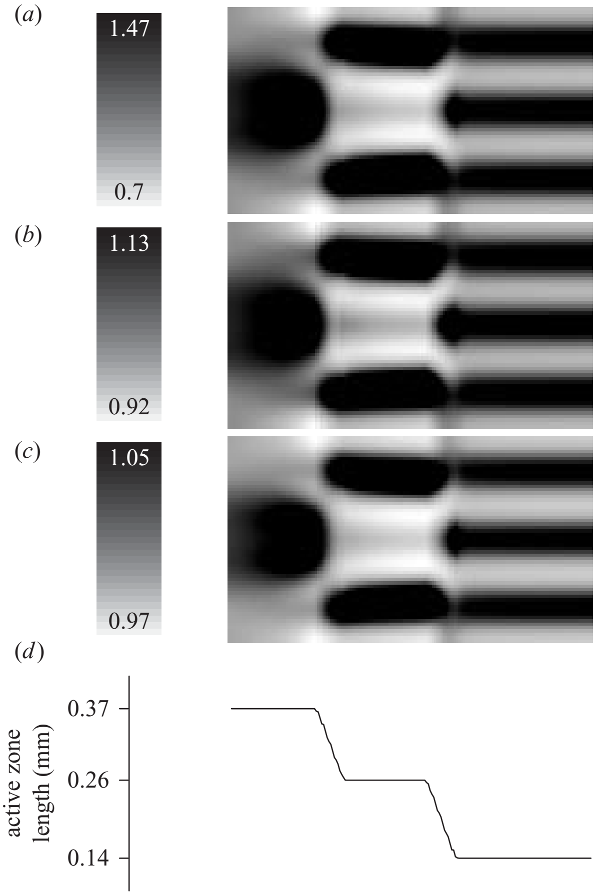

Figure 2. Typical results of numerical integration of equations (8.2)–(8.4) for (*a*) the TGF-β, (*b*) inhibitor and (*c*) cell density. (*d*) The proximodistal length of the apical zone as a fraction of its anteroposterior width. The left-hand scales in (*a*)–(*c*) represent the concentrations as a fraction of the equilibrium concentrations (i.e. 1.0 = equilibrium). Note that the variations in the AER are smooth and the apparent discontinuities in the resulting skeletal structures seen in the figure (humerus, radius and ulna, and digits) are a result of the fact that the changes in stability of the different patterns occur on a very short time-scale compared with growth. (The FGF concentration in the active zone is assumed to be constant in these simulations as a result of release by the dorsal and ventral ectoderm. The numerical method was an explicit finite difference scheme. The plot has 80 × 159 grid points.)

unity, except for $D_i/D_a \approx 10$ to ensure that pattern-forming instabilities appear and $g \gg 1$ to ensure that these patterns are of the correct size (very roughly linear stability analysis suggests the number of pattern features is of the order $\sqrt{g}/(2\pi)$).

We used the following parameters and functions for the activator–inhibitor dynamics in simulations for figure 3*a*:

$$d = 10.0,\ g = 4500,\ \tilde{\mathcal{J}}_a(u) = \frac{15.5417\,u}{3.42421 + u},$$
$$\tilde{\mathcal{J}}_i(u) = \frac{17.3913\,u}{3.68261 + u}, \qquad \tilde{\mathcal{J}}_a^1 \alpha(u_{eq}) = 0.03,$$
$$\beta(u) = \frac{2.76744\,u}{7.14 + 3.71395\,u}. \tag{8.6}$$

These choices are based on the assumption of Michaelis–Menten first-order dynamics for the activator and inhibitor.

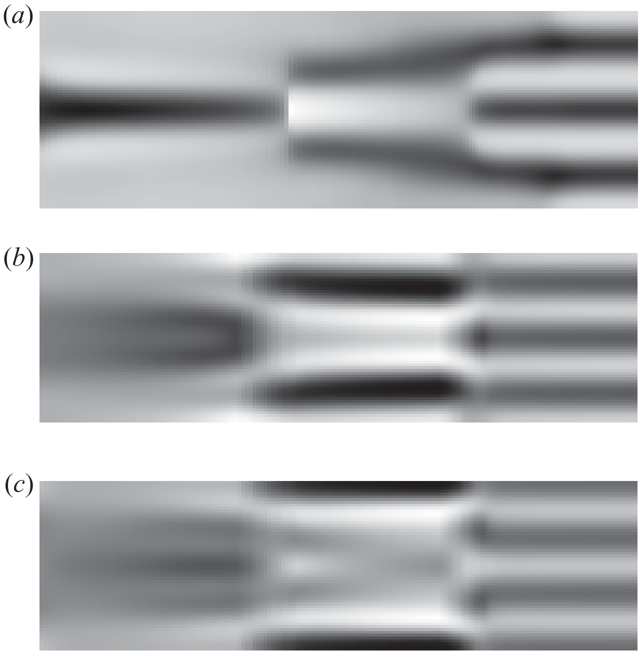

Figure 3. Typical examples of skeletal structures allowing for growth. After the initial cellular condensations form (as seen in figure 2), we have assumed that growth occurs at a constant rate. Consequently, earlier condensations (as well as cartilage elements) are subject to more growth than later ones. The skeletal form depends on parameter values, time-dependent changes in the active zone and initial conditions. In (*a*) several modes can grow, whereas only a few can grow in (*b*) and (*c*). The influence of initial conditions on the final form can be seen in (*b*) and (*c*), which have the same parameter values but different initial conditions. All these properties must be selected for by evolution to achieve a specific skeletal form.

Other choices can be made in the light of future knowledge of the biochemistry involved, but we believe that though these choices will affect the results quantitatively, they will not change the system's generic qualitative behaviour. There is a unique equilibrium (u_{eq}, v_{eq}, R_{eq}). It is given by $u_{eq} = 1.100$, $v_{eq} = 0.986$ and $R_{eq} = 1.0$. For the cell dynamics, we used the following parameters:

$$d_{cell} = 0.1, = \tilde{\lambda}_2 = 1.366, \gamma(u) = \frac{0.116279\,u}{7.14 + 3.71395\,u}, \ \tilde{r} = 20.0. \tag{8.7}$$

It is worth noting in equation (8.4) that the dependence of $d_{effective}$ on the concentration u is relatively weak for our choice of parameters. In particular, the effective diffusion coefficient is always positive. (For example, the effective cell diffusion coefficient at $u = u_{eq}$ and $R = R_{eq}$ is $d_{effective} = [d_{cell} - \tilde{\lambda}_2 \gamma(u) R] = 0.084$; whereas at $u = 0.1\ u_{eq}$, $R = R_{eq}$, we have $d_{effective} = 0.098$, and at $u = 2\ u_{eq}$, $R = R_{eq}$, we have $d_{effective} = 0.077$.)

We have solved equations (8.2)–(8.4) numerically on a moving rectangle $\Omega(t)$ of constant scaled width 1.0 in the y-direction and time-varying active-zone length $\ell(t)$ in the x-direction. We used an explicit Euler forward finite difference scheme, typically using 80 × 159 grid points, taking care to choose time steps such that numerical diffusive instabilities did not occur.

How should the active zone vary with time? The linear patterning modes have the form $W_{mn}(x, y) = \cos(\pi m y)\cos((\pi(n + 0.5)/\ell)x)$, and therefore to create k skeletal elements in the anteroposterior direction we need to select $m = 2k$, because the mode m creates $m + 1$ half-periods of high and low activator concentration, and k skeletal elements require $2k + 1$ such variations. The eigenvalue, n, is less critical in creating anteroposterior structure but could affect proximodistal structural variations.

Thus the active zone has to change in such a manner as to select the desired skeletal features. In particular, if we want one skeletal element (the 'humerus') followed by two skeletal elements (the 'radius' and 'ulna') followed by three 'digits', then we need to choose the biological parameters carefully (presumably, this choice has occurred biologically by evolution), so that we achieve a sequence of active zone proximodistal to anteroposterior length-scale ratios $\ell_1 \rightarrow \ell_2 \rightarrow \ell_3$ such that:

$$(m_1, n_1) = (2, 2) \text{ is subject to exponential growth for } \ell_1, \tag{8.8}$$

$$(m_2, n_2) = (4, 1) \text{ is subject to exponential growth for } \ell_2, \tag{8.9}$$

$$(m_3, n_3) = (6, 0) \text{ is subject to exponential growth for } \ell_3. \tag{8.10}$$

We selected these structures computationally by reducing the active zone length, so that the key linear modes we need grow with time. We chose to reduce the active zone length in a piecewise constant fashion. That is, there are periods during which the active zone length λ and apical zone length λ_{apical} are constant while we allow the frozen zone to grow with a steady velocity v_{growth}. Then, on a very short time-scale, we reduce ℓ by increasing the size of the proximal frozen zone (the apical zone size remaining constant). These dynamics can be specified by a sequence of active zone ratios ℓ and associated time intervals τ, during which time the active zone ratio does not change. This choice is certainly not unique and could be altered in the light of new biological information (for example, we could allow the change in active zone length to occur at a specified rate). We chose the length $\ell(t)$ to be a decreasing function of time; it drops for the simulation in figure 3*a* from $\ell_1 = 0.39$ to $\ell_2 = 0.31$ to $\ell_3 = 0.21$; in each case for approximately the same time interval, τ (see also the graph at the bottom of figure 2). It is interesting to note that the resulting selected patterns do not have very large spatial gradients and are therefore consistent with the gradient expansion methods we used in deriving equation (8.2).

In electronic Appendix B we perform a linear stability analysis of equations (8.2)–(8.4). Using the parameters above, we find that as a function of wavenumber k, the largest eigenvalue $\lambda_{\max}$ (k^2) is positive in the interval of k^2 between [135.3, 801.4]. If a mode $k^2{}_{mn}$ falls into this interval, it will grow with time. We note that if the interval $[K_{\min}, K_{\max}]$ is small, only very few of the eigenvalues k^2_{mn} will fall into this interval. So, in such cases, the growing modes can be selected quite precisely, and if these linear modes represent the incipient skeletal form, then we might expect a biologically robust structure to develop (see figure 3*b*,*c*). If, however, the interval $[K_{\min}, K_{\max}]$ is large, many modes will grow. In such cases, the structures that can develop are quite diverse and in general their selection is much less robust. (Robustness of pattern selection could presumably be achieved in such cases by secondary molecular stabilizing mechanisms.) At the same time, combinations of growing modes with comparable temporal growth rates allow for biologically more realistic patterns (see figure 3*a*). For the specific parameters above (corresponding to figure 3*a*), typically several such modes occur (see tables 1–3, electronic Appendix B). Therefore, although in general we can ensure that the required sequence of modes grow, other modes will also appear. Thus we expect the final form to be more complex than a simple linear mode analysis would suggest.

Figure 3*b*,*c* illustrates the importance of the initial conditions for the final outcome, as these two simulations were made with the same set of parameters, and differ only in the chosen initial conditions. Note that the third group of segements (the 'digits') are negatives of each other, i.e. dark stripes in one correspond to light stripes in the other and vice versa. In the linear analysis, the two functions differ only in the sign (+ or −).

The AER and dorsal and ventral limb ectoderm are directly underlain by a hyaluronan-rich matrix which is inhibitory to cell condensation during the patterning stages (Solursh *et al.* 1981; Solursh & Reiter 1988). This inhibition (along with the inhibitory effect of ecotodermal FGFs on condensation (Moftah *et al.* 2002)) would tend to suppress solutions to equations (8.1)–(8.3) that resulted in condensations at the boundary, making the selection of biologically relevant patterns less subject to the choice of initial conditions.

We ran the simulations in the time interval $t = 0$ to $t = 2.0$, in scaled units. The nonlinear active zone dynamics change the predictions of linear stability analysis, in that the modes saturate with respect to concentration in contrast to the continual growth or decay that linear stability analysis predicts. Additionally, the emerging patterns are affected by the fact that the reactor–diffusion domain is moving. In fact, the speed of change of the active zone is an important parameter; our computer simulations have shown that different speeds can give rise to very different patterns.

We see from figure 3 that, as the ratio of the proximodistal length to anteroposterior width ℓ of the active zone decreases, the number of skeletal elements along the anteroposterior length increases. This relation might seem strange at first; indeed it is not obvious why, in general, shortening the proximodistal length of the active zone should give rise to more pattern elements along the anteroposterior fixed length.

The reason is best seen by looking at the linear stability analysis. We are interested in patterns that have m half-periods along the anteroposterior length and n half-periods along the proximodistal length. The corresponding wavenumber on a rectangle of proximodistal length ℓ and anteroposterior length 1 (in scaled units) is $k^2_{mm} = \pi(m^2 + ((n + 1/2)/\ell)^2)$. Only those patterns for which the wavenumber k^2_{mn} falls into a certain small fixed interval controlled by the biology will undergo exponential growth. So, for the three consecutive and decreasing proximodistal lengths $\ell_1 > \ell_2 > \ell_3$ we used to generate figure 3, we must have:

$$m_s^2 + ((n_s + 1/2)/\ell)^2 \approx \text{const}, \tag{8.11}$$

for $s = 1, 2, 3$, where the constant only depends on the reaction kinetics (not on the geometry). When ℓ is small enough, only $n = 0$ will solve equation (8.11), and thus it is natural to assume that $n_3 = 0$, i.e. the final pattern is essentially homogeneous along the proximodistal axis and consist of 'digits'. Thus the above constant equals $m_3^2 + 1/(4\ell_3^2)$ where m_3 is the number of 'digits'. For $s = 1$ or 2, $n_s > 0$ is also a solution. Then the number of elements m_s along the anteroposterior axis is less than the corresponding number of digits m_3. Clearly, at small ℓ ratios, 'digits' are the only available growing mode, but at large ℓ ratios, more pattern-forming modes exist and selection must be based on a combination of initial conditions, and interactions with biomolecules such as FGFs and hyaluronan that inhibit chondrogenesis near the ectoderm.

9. DISCUSSION

The dynamical system described by equation (6.1) represents a 'bare bones' mechanism for limb skeletal development in that it incorporates a core set of cellular–biochemical processes known to occur in limb bud mesenchyme. Further sculpting of the skeletal form would be necessary (and perfectly consistent with the above scheme) to introduce additional structural features. In particular, differences in the character of the skeletal elements across the anteroposterior axis, or in the contours of individual elements along their dorsoventral axis, could be caused by non-uniformly distributed gene products such as Sonic hedgehog, Hox and Wnt proteins, which may alter cell response to the activators and inhibitors considered in our model. Another model for skeletogenesis has been proposed based on cell traction forces generated by mobile mesenchymal cells (Oster *et al.* 1983); however, we believe diffusible signals coupled to haptotaxis better reflect current knowledge of the molecular mechanisms of mesenchymal pattern formation in the limb.

There are other general issues that will influence growth and form during skeletal development. Thus, although partial differential equations are very appropriate to investigate large scales, it is clear that at distances of a few cell diameters, this continuum approach must break down. At smaller scales, point cell approaches (cellular automata (e.g. Kiskowski *et al.* 2004)) and extended cell models such as the Cellular Potts models (e.g. Izaguirre *et al.* 2004) will be needed. We have assumed that the ECM is homogeneous, and that the differentiated cells have similar diffusion constants. Clear evidence to the contrary should be incorporated into future simulations. The same point applies to our use of rectangular geometry and zero-flux boundary conditions. The influence of limb contours creating convex and concave reactor–diffusion chambers is now under active investigation, and will be reported in a future publication. A further point should be made. The skeletal elements themselves, once formed, will provide obstacles and boundaries for the operation of further activator–inhibitor and cell–cell interactions in the developing limb, which will influence phenomena not considered in the 'bare bones' model, such as interdigital cell death, formation of limb musculature and innervation of the limb.

Species-specific carpal and tarsal structures of the wrist and ankle need to be investigated further. These may form because of transitions from stripe-like to spot-stripe patterns which can occur in this class of equations (Shoji *et al.* 2003). We suggest that integration of knowledge of cellular and biochemical processes of development with dynamical modelling, geometry and computational strategies will prove useful in understanding limb skeletal development at a more detailed level, as well as other aspects of organogenesis.

This work was supported by NSF grants no. IBN-0083653 to J.A.G., H.G.E.H. and S.A.N., and no. IBN-0090499 to S.A.N. We acknowledge support from the Center for Applied Mathematics and the Interdisciplinary Center for the Study of Biocomplexity at the University of Notre Dame and the Biocomplexity Institute at Indiana University. J.A.G. acknowledges additional support from an Indiana University Pervasive Technologies Laboratories fellowship and an IBM Innovation Institute award and NASA grant NAG 2-1619. We also thank the referees for their many useful comments.

ENDNOTES

[1] What was actually found is that TGF-β2 upregulates its own production by the cell, rather than acting as a classical autocatalytic chemical species. It is therefore in this sense of upregulating a biosynthetic process that we use the term 'activator' in this paper.

[2] Again we use the term 'inhibitor' to mean a chemical that downregulates a biosynthetic process.

[3] We use this term in preference to 'reaction–diffusion' to point out that the active component is not a chemical reaction but a living cell with complex response functions.

REFERENCES

Canalis, E., Economides, A. N. & Gazzerro, E. 2003 Bone morphogenetic proteins, their antagonists, and the skeleton. *Endocr. Rev.* **24**, 218–235.

Crampin, E. J., Hackborn, W. W. & Maini, P. K. 2002*a* Pattern formation in reaction–diffusion models with non-uniform domain growth. *Bull. Math. Biol.* **64**, 747–769.

Crampin, E. J., Gaffney, E. A. & Maini, P. K. 2002*b* Mode-doubling and tripling in reaction–diffusion patterns on growing domains: a piecewise linear model. *J. Math. Biol.* **44**, 107–128.

Dillon, R. & Othmer, H. G. 1999 A mathematical model for outgrowth and spatial patterning of the vertebrate limb bud. *J. Theor. Biol.* **197**, 295–330.

Downie, S. & Newman, S. 1994 Morphogenetic difference between fore and hind limb precartilage mesenchemy: relation to mechanisms of skeletal pattern formation. *Devl Biol.* **162**, 195–208.

Downie, S. & Newman, S. 1995 Different roles for fibronectin in the generation of fore and hind limb precartilage condensations. *Devl Biol.* **172**, 519–530.

Fallon, J. F., Lopez, A., Ros, M. A., Savage, M. P., Olwin, B. B. & Simandl, B. K. 1994 FGF-2: apical ectodermal ridge growth signal for chick limb development. *Science* **264**, 104–107.

Frenz, D., Akiyama, S., Paulsen, D. & Newman, S. 1989*a* Latex beads as probes of cell surface–extracellular matrix interactions during chondrogenesis: evidence for a role for amino-terminal heparin-binding domain of fibronectin. *Devl Biol.* **136**, 87–96.

Frenz, D., Jaikaria, N. & Newman, S. 1989*b* The mechanism of precartilage mesenchymal condensation: a major role for interaction of the cell surface with the amino-terminal heparin-binding of fibronectin. *Devl Biol.* **136**, 97–103.

Hall, B. & Miyake, T. 2000 All for one and one for all: condensations and the initiation of skeletal development. *Bioessays* **22**, 138–147.

Hamburger, V. & Hamilton, H. L. 1951 A series of normal stages in the development of the chick embryo. *J. Morphol.* **88**, 49–92.

Izaguirre, J. A. (and 10 others) 2004 COMPUCELL, a multi-model framework for simulation of morphogenesis. *Bioinformatics* **20**, 1129–1137.

Kiskowski, M. A., Alber, M. S., Thomas, G. L., Glazier, J. A., Bronstein, N. B., Pu, J. & Newman, S. A. 2004 Interplay between activator-inhibitor coupling and cell-matrix adhesion in a cellular automaton model for chondrogenic patterning. *Devl Biol.* **271**, 372–387.

Kosher, R. A., Savage, M. P. & Chan, S. C. 1979 *In vitro* studies on the morphogenesis and differentiation of the mesoderm subjacent to the apical ectodermal ridge of the embryonic chick limb-bud. *J. Embryol. Exp. Morphol.* **50**, 75–97.

Leonard, C., Fuld, H., Frenz, D., Downie, S., Massagué, J. & Newman, S. 1991 Role of transforming growth factor-beta in chondrogenic pattern formation in the embryonic limb: stimulation of mesenchymal condensation and fibronectin gene expression by exogenous TGF-β and evidence for endogenous TGF-beta-like activity. *Devl Biol.* **145**, 99–109.

Lewis, J. H. 1975 Fate maps and the pattern of cell division: a calculation for the chick wing-bud. *J. Embryol. Exp. Morphol.* **33**, 419–434.

Martin, G. R. 1998 The roles of FGFs in the early development of vertebrate limbs. *Genes Dev.* **12**, 157–186.

Miura, T. & Shiota, K. 2000*a* The extracellular matrix environment influences chondrogenic pattern formation in limb micromass culture: experimental verification of theoretical models of morphogenesis. *Anat. Rec.* **258**, 100–107.

Miura, T. & Shiota, K. 2000*b* TGFβ-2 acts as an activator molecule in reaction−diffusion model and is involved in cell sorting phenomenon in mouse limb micromass culture. *Devl Dynam.* **217**, 241–249.

Miura, T., Komori, M. & Shiota, K. 2000 A novel method for analysis of the periodicity of chondrogenic patterns in limb bud cell culture: correlation of *in vitro* pattern formation with theoretical models. *Anat. Embryol.* **201**, 419–428.

Moftah, M. Z., Downie, S. A., Bronstein, N. B., Mezentseva, N., Pu, J., Maher, P. A. & Newman, S. A. 2002 Ectodermal FGFs induce perinodular inhibition of limb chondrogenesis *in vitro* and *in vivo* via FGFs via FGF receptor2. *Devl Biol.* **249**, 270–282.

Newman, S. A. 1996 Sticky fingers: Hox genes and cell adhesion in vertebrate limb development. *Bioessays* **18**, 171–174.

Newman, S. & Frisch, H. 1979 Dynamics of skeletal pattern formation in developing chick limb. *Science* **205**, 662–668.

Newman, S. A. & Tomasek, J. J. 1996 Morphogenesis of connective tissues. In *Extracellular matrix, vol. 2: molecular components and interactions* (ed. W. D. Comper), pp. 335–369. Amsterdam: Harwood Academic Publishers.

Newman, S., Frisch, H. & Percus, J. K. 1988 On the stationary state analysis of reaction–diffusion mechanisms for biological pattern formation. *J. Theor. Biol.* **134**, 183–197.

Niswander, L., Tickle, C., Vogel, A., Booth, I. & Martin, G. R. 1993 FGF-4 replaces the apical ectodermal ridge and directs outgrowth and patterning of the limb. *Cell* **75**, 579–587.

Oberlender, S. A. & Tuan, R. S. 1994 Expression and functional involvement of N-cadherin in embryonic limb chondrogenesis. *Development* **120**, 177–187.

Ornitz, D. M. & Marie, P. J. 2002 FGF signaling pathways in endochondral and intramembranous bone development and human genetic disease. *Genes Dev.* **16**, 1446–1465.

Oster, G. F., Murray, J. D. & Harris, A. K. 1983 Mechanical aspects of mesenchymal morphogenesis. *J. Embryol. Exp. Morphol.* **78**, 83–125.

Peters, K. G., Werner, S., Chen, G. & Williams, L. T. 1992 Two FGF receptor genes are differentially expressed in epithelial and mesenchymal tissues during limb formation and organogenesis in the mouse. *Development* **114**, 233–243.

Saunders, J. W. Jr 1948 The proximo–distal sequence of origin of the parts of the chick wing and the role of the ectoderm. *J. Exp. Zool.* **108**, 363–402.

Sela-Donenfeld, D. & Kalcheim, C. 2002 Localized BMP4–noggin interactions generate the dynamic patterning of noggin expression in somites. *Devl Biol.* **246**, 311–328.

Shoji, H., Iwasa, Y. & Kondo, S. 2003 Stripes, spots or reversed spots in two-dimensional Turing systems. *J. Theor. Biol.* **244**, 339–350.

Solursh, M. & Reiter, R. S. 1988 Inhibitory and stimulatory effects of limb ectoderm on *in vitro* chondrogenesis. *J. Exp. Zool.* **248**, 147–154.

Solursh, M., Singley, C. T. & Reiter, R. S. 1981 The influence of epithelia on cartilage and loose connective tissue formation by limb mesenchyme cultures. *Devl Biol.* **86**, 471–482.

Szebenyi, G., Savage, M. P., Olwin, B. B. & Fallon, J. F. 1995 Changes in the expression of fibroblast growth factor receptors mark distinct stages of chondrogenesis *in vitro* and during chick limb skeletal patterning. *Devl Dynam.* **204**, 446–456.

Thannickal, V. J., Aldweib, K. D., Rajan, R. & Fanburg, B. L. 1998 Upregulated expression of fibroblast growth factor (FGF) receptors by transforming growth factor-beta1 (TGF-β1) mediates enhanced mitogenic responses to FGFs in cultured human lung fibroblasts. *Biochem. Biophys. Res. Commun.* **251**, 437–441.

Tickle, C. 2003 Patterning systems: from one end of the limb to the other. *Dev. Cell* **4**, 449–458.

Tomasek, J., Mazurkiewicz, J. & Newman, S. 1982 Non-uniform distribution of fibronectin during avian limb development. *Devl Biol.* **90**, 118–126.

Tsonis, P. A., Del-Rio-Tsonis, K., Millan, J. L. & Wheelock, M. J. 1994 Expression of N-cadherin and alkaline phosphatase in chick limb bud mesenchymal cells: regulation by 1,25-dihydroxyvitamin *D*3 or *TGF*β1. *Exp. Cell. Res.* **213**, 433–437.

Turing, A. 1952 The chemical basis of morphogenesis. *Phil. Trans. R. Soc. Lond.* B **237**, 37–72.

Van Obberghen-Schilling, E., Roche, N. S., Flanders, K. C., Sporn, M. B. & Roberts, A. 1988 Transforming growth factor β-1 positively regulates its own expression in normal and transformed cells. *J. Biol. Chem.* **263**, 7741–7746.

Zeng, W., Thomas, G. L., Newman, S. A. & Glazier, J. A. 2003 A novel mechanism for mesenchymal condensation during limb chondrogenesis *in vitro*. In *Mathematical modelling and computing in biology and medicine, 5th ESMTB Conference, 2002* (ed. V. Capasso), pp. 80–86. Bologna, Italy: Esculapio Publishing Co.

As this paper exceeds the maximum length normally permitted, the authors have agreed to contribute to production costs.

Visit www.journals.royalsoc.ac.uk and navigate to this article through *Proceedings*: Biological Sciences to see the accompanying electronic appendices.